Electrochemical Corrosion Behavior of HiPIMS-Deposited Diamond-Like Carbon (DLC) Coatings on AISI 52100 Steel in Synthetic Seawater

Ilse Arreola , Engelbert Huape , Martin Flores , Héctor Carreón , José Bernal , Ariosto Medina *

Posted Date: 30 April 2026

doi: 10.20944/preprints202604.2121.v1

Keywords: DLC; HiPIMS; AISI 52100; EIS; porosity; Raman

Article

Electrochemical Corrosion Behavior of HiPIMS-Deposited Diamond-like Carbon (DLC) Coatings on AISI 52100 Steel in Synthetic Seawater

Ilse Arreola [1], Engelbert Huape [2], Martin Flores [3], Héctor Carreón [1], José Bernal [4] and Ariosto Medina [1,*]

[1] UMSNH. Institute of Research in Metallurgy and Materials, Morelia, Mexico
[2] UMSNH. Faculty of Mechanical Engineering, Morelia, Mexico
[3] Department of Project Engineering, CUCEI, University of Guadalajara, Zapopan, Mexico
[4] National Technological Institute of Mexico/Technological Institute of Orizaba, Orizaba, Mexico
* Correspondence: ariosto.medina@umich.mx

Abstract

This manuscript evaluates the electrochemical corrosion resistance of diamond-like carbon (DLC) coatings deposited via High-Power Impulse Magnetron Sputtering (HiPIMS) on AISI 52100 steel in synthetic seawater. While AISI 52100 steel is valued for its hardness, it is highly susceptible to localized and uniform corrosion in chloride-rich marine environments. In this study, samples were characterized using Raman spectroscopy to analyze sp^2/sp^3 bonding, and their corrosion behavior was assessed through potentiodynamic polarization, linear polarization resistance (LPR), and electrochemical impedance spectroscopy (EIS) over 24 hours of immersion. Results demonstrated that the DLC coatings significantly enhanced electrochemical stability, shifting corrosion potentials toward more noble values and reducing corrosion current densities by several orders of magnitude compared to the uncoated substrate. EIS data revealed high polarization resistance and effective barrier properties, despite a calculated total porosity of 3.06% resulting from intrinsic micro-defects. Although localized subsurface degradation and minor flaking were observed at defect sites, the HiPIMS-deposited DLC coatings effectively mitigated the corrosive impact of synthetic seawater, providing a robust protective barrier for high-precision steel components.

Keywords: DLC; HiPIMS; AISI 52100; EIS; porosity; Raman

---

1. Introduction

AISI 52100 steel is a high-carbon, chromium alloy extensively utilized in the bearing industry due to its exceptional hardness, wear resistance, and contact fatigue strength. Its microstructure is a determining factor in withstanding severe dynamic loading conditions. However, the surface integrity, mechanical and tribological performance of this material are closely dependent on chemical composition, geometric and microstructural variations; those induced during grinding and finishing processes can compromise its stability. Consequently, the optimization of heat treatments and the control of surface roughness are critical factors to maximize toughness and minimize premature failures caused by pitting or fatigue in high-precision components manufactured from this alloy [1,2].

Furthermore, finishing technologies have undergone significant evolution; Diamond-Like Carbon (DLC) coatings represent a class of amorphous carbon materials that exhibit exceptional mechanical and tribological properties analogous to those of natural diamond. These coatings are characterized by a metastable structure comprising a mixture of tetrahedrally coordinated (sp^3) and trigonally coordinated (sp^2) carbon bonds, the relative ratio of which determines the film's hardness, chemical inertness, and thermal stability. Due to its high density and compact nature, DLC serves as a highly effective diffusion barrier, providing superior protection against wear and corrosion in aggressive environments. Additionally, its low friction coefficient and biocompatibility render a critical technical solution, for optimizing the performance of high-precision mechanical components and biomedical devices [3].

However, the performance is not solely dependent on external processes; the chemical composition and internal microstructure of the steel play a decisive role. Recent investigations confirm that precise tailored heat treatments to balance hardness and the distribution of spherical carbides is fundamental to mitigate frictional wear. High-Power Impulse Magnetron Sputtering (HiPIMS) with positive pulses represents an advanced evolution of Physical Vapor Deposition (PVD) techniques for the synthesis of Diamond-Like Carbon (DLC) coatings. This technical variant overcomes the critical limitation of poor adhesion on metallic substrates by promoting more robust chemical bonding and a more homogeneous stress distribution [4,5].

The functionality of Diamond-Like Carbon (DLC) coatings relies on comprehensive substrate preparation to overcome poor interfacial adhesion. Prior thermal and thermochemical treatments, such as plasma nitriding and carburizing, are essential to establish a hardened support layer that prevents coating collapse under high-load conditions. In addition, pretreatments including shot peening and chemical etching are employed to remove soft metallic phases and optimize surface roughness. These processes, combined with in situ ion bombardment cleaning, reduce the hardness gradient between the substrate and the DLC layer, thereby minimizing residual stresses and ensuring the structural integrity of the system in cutting applications and high-precision components [6,7].

AISI 52100 steel is an alloy widely valued in engineering for its exceptional hardness, high wear resistance and fatigue strength; however, it exhibits an intrinsic vulnerability to electrochemical degradation in aggressive environments. In corrosive media, such as saline solutions (synthetic seawater or NaCl) and humid industrial atmospheres, this material undergoes accelerated oxidation processes and localized corrosion (pitting). Since the surface integrity is critical to its mechanical performance, the implementation of nanostructured coatings and amorphous carbon films emerges as an essential strategy. These barriers not only mitigate the diffusion of corrosive agents toward the substrate but also preserve the steel’s tribological properties, preventing premature failure caused by the synergy between mechanical wear and chemical corrosion [8].

Diamond-like carbon (DLC) coatings have established themselves as an advanced solution for mitigating the degradation of surface and metallic components. In terms of corrosion, these coatings act as a highly effective physical barrier that impedes the diffusion of aggressive species, such as chloride ions (Cl^-), toward the metallic substrate. However, the efficacy of this protection is intrinsically linked to the film morphology and the absence of structural defects or porosity, which could otherwise induce localized corrosion. The incorporation of dopants and the utilization of ionic liquids as complementary lubricants have been shown to significantly enhance the electrochemical stability of the system, reducing not only the friction coefficient but also the susceptibility to oxidation in severe industrial and marine environments [9].

The protection of high-alloy 100Cr6 (AISI 52100) steel in marine environments represents a significant improvement and a critical challenge due to the aggressive chlorine ions environment , which promote pitting corrosion and accelerated material degradation. The implementation of tungsten-doped diamond-like carbon (W-DLC) coatings via physical vapor deposition (PVD) techniques offers a robust solution by creating a hydrophobic, inert barrier that drastically increases the polarization resistance of the system. In contact with synthetic seawater, this coating reduces the corrosion current density and elevates the pitting potential, preventing electrolyte penetration to the substrate interface. This synergy between metallic doping and the amorphous carbon matrix not only mitigates anodic dissolution but also preserves the structural integrity of the component under combined conditions of mechanical wear and saline chemical attack [10].

The study of Diamond-Like Carbon (DLC) coatings has diversified to address limitations regarding adhesion and stability, focusing on the utilization of High-Power Impulse Magnetron Sputtering (HiPIMS) with positive pulses and Plasma Immersion Ion Implantation (PIII)

doi:10.20944/preprints202604.2121.v1

pretreatments to optimize the coating-substrate interface. Both pure layers and metal-doped systems (such as Tungsten or Chromium) have been evaluated on high-demand substrates, including AISI 52100 (100Cr6) steel and tungsten carbide. The evaluation frameworks range from the analysis of surface integrity and waviness in manufacturing processes, to performance testing in highly corrosive media, such as synthetic seawater [11]. This study evaluates, the electrochemical corrosion of Diamond-Like Carbon coatings (DLC) deposited by High-Power Impulse Magnetron Sputtering (HiPIMS). This research focuses specifically on the role of steel substrate and its subsequent impact on the coating's integrity when exposed to synthetic seawater.

2. Materials and Methods

Experiments were conducted using AISI 52100 steel (as-received condition, M1), machined into disc-shaped specimens with dimensions of 25.4 mm in diameter and 5 mm in thickness. The samples underwent a hardening heat treatment (M2 – HT) consisting of austenitizing at 864 °C for 20 min, followed by oil quenching, to induce a predominantly martensitic microstructure and enhance surface hardness. Surface preparation was performed through progressive grinding with silicon carbide (SiC) abrasive papers up to 2000 grit, followed by fine polishing using polycrystalline diamond suspensions of 6 µm, 3 µm, and 0.05 µm, achieving a target average surface roughness of Ra ≤ 10 nm.

Subsequently, the specimens underwent sequential ultrasonic cleaning in acetone and isopropyl alcohol for 15 min to eliminate abrasive residues and surface contaminants. Drying was performed using a gaseous nitrogen flow. Both the steel samples and the silicon (Si) reference substrates were then loaded into the deposition system's vacuum chamber, ensuring controlled conditions prior to the diamond-like carbon (DLC) coating growth process (M3 – DLC). Upon reaching the operating vacuum conditions within the chamber, the samples were subjected to an argon (Ar) plasma etching pretreatment to remove residual contaminants and activate the surface.

Subsequently, a combined Ar + Cr ion bombardment was applied to enhance the substrate surface energy and promote interfacial adhesion of the DLC coating onto the AISI 52100 steel. The specific experimental parameters employed during the coating deposition process are detailed in Table 1.

Table 1. Parameters used for the deposition of DLC coatings on AISI 52100 steel using HiPIMS.

Parameters	Etching Ar+	Etching + Cr	CrC	DLC
Voltage (V)	700	700/702	702/690	700
Current (mA)	4	4/284	313/36	36
Power (W)	3	3/200	219/23	25
Pulse amplitude (ms)	50	50/200	200/50	50
Frequency (Hz)	300	300/300	300/300	300
FAR (sccm)	10	10	10	10
Pressure (Torr)	3.61 x 10-3	3.14 x 10-3	3.09 x 10-3	3.53 x 10-3
Time (s)	1800	1800	2400	2400

During the deposition process, silicon (Si) substrates were positioned to facilitate cross-sectional imaging, film thickness measurement, and coating uniformity analysis. These evaluations were performed using a JEOL JSM-7600F Scanning Electron Microscope (SEM), equipped with a Bruker XFlash 630 Energy Dispersive X-ray Spectroscopy (EDS) detector. The structural nature of the DLC coatings deposited on the AISI 52100 steel substrates were characterized by identifying and analyzing the characteristic D and G bands via Raman Spectroscopy. Measurements were conducted using a Thermo Fisher Scientific DXR confocal Raman microscope, utilizing a 532 nm laser as the excitation source.

Electrochemical tests were conducted using a computer-controlled ACM Instruments potentiostat. All potentials were measured against a saturated calomel electrode (SCE) as the reference electrode, with a graphite rod serving as the counter electrode. Experiments were performed at room temperature using an electrolytic cell volume of 60 mL. The electrochemical characterization included potentiodynamic polarization curves, linear polarization resistance (LPR) and electrochemical impedance spectroscopy (EIS). Corrosion rates were determined based on the corrosion current density (i_{corr}) calculated from the LPR measurements. Potentiodynamic polarization curves were obtained by sweeping the applied potential from -500 mV to +1500 mV versus the open circuit potential (OCP) at a scan rate of 1 mV/s, in accordance with ASTM G3-89 a stabilization period of 60 min was established to reach a steady state prior to the commencement of the electrochemical tests. EIS measurements were performed using a sinusoidal signal with an amplitude of 20 mV vs. OCP over a frequency range from 0.05 Hz to 10 kHz, with data acquired at 30 min, 12 h, and 24 h of immersion. LPR measurements were recorded by polarizing the specimen from +15 to -15 mV vs. OCP at a scan rate of 1 mV/s every 15 min for 24 h. Finally, the corrosion products of the as-cast samples were analyzed via scanning electron microscopy (SEM) and energy-dispersive X-ray spectroscopy (EDS).

Electrochemical tests were conducted using simulated seawater as the electrolytic medium to replicate representative exposure conditions in controlled marine environments. The electrolyte was prepared by sequentially dissolving the salts specified by the standard in distilled water, adhering to the established order of incorporation and maintaining constant stirring to ensure the complete solubilization of each component and the homogeneity of the final solution. Table 2 presents the chemical composition recommended by the ASTM D1141 standard for the preparation of 1 L of solution, which served as the electrolytic medium in the experimental trials.

Table 2. Reagents and quantities used for the preparation of seawater.

Reagent	Quantity (g/L)
Sodium chloride	24.53
Sodium sulfate (anhydrous)	4.09
Magnesium chloride hexahydrate	5.20
Calcium chloride (anhydrous)	1.16
Strontium chloride hexahydrate	0.025
Potassium chloride	0.695
Sodium bicarbonate	0.201
Potassium bromide	0.101
Boric acid	0.027
Sodium fluoride	0.003

Once all salts were fully dissolved, the solution pH was adjusted to 8.2±0.2 using NaOH. This pH value is representative of natural seawater, allowing for a more accurate correlation with real-world exposure conditions.

Based on the linear polarization resistance (LPR) results, the kinetic corrosion rate was calculated in accordance with the ASTM G102 standard, where the corrosion rate is expressed as Equation 1:

$$VC = k(i_{corr}/\rho)\ EW, \tag{1}$$

Where EW is the equivalent weight of the alloy, i_{corr} represents the corrosion current density, ρ denotes the alloy density, and K is a constant. The equivalent weight was determined using Equations 2 and 3.

$$EW = 1/Q, \tag{2}$$

$$Q = \Sigma(n_i f_i/W_i), \tag{3}$$

Where f_i is the mass fraction of the *ith* element in the alloy, W_i represents the atomic weight of the *ith* element, and n_i denotes the valence of the *ith* element. The corrosion current density was determined from the polarization resistance measurements as follows:

$$i_{corr} = \beta / R_p, \tag{4}$$

Where β is the Stern–Geary constant, which was determined from the anodic and cathodic Tafel slopes using Equation 5:

$$\beta = \beta_a \beta_c / 2.303(\beta a + \beta c), \tag{5}$$

3. Results

3.1. Characterization of DLC Coating

Figure 1 illustrates the Raman spectra for samples M1, M2, and M3. Low-frequency signals associated with the as-received material (M1) are observed, which correlate with the reported crystalline phases of 52100 steel and those induced by the M2 heat treatment. In contrast, M3 exhibits the characteristic amorphous carbon profile, defined by the overlap of the D and G bands (~1350 cm^{-1} and ~1580 cm^{-1}, respectively), reflecting the coexistence of sp^2 and sp^3 hybridized carbon clusters [12,13]. In this regard, the G band arising from the stretching of sp^2 bonds along with its full width at half maximum (FWHM) and peak position, serves as a critical indicator of thermal stability and the diamond-like bond fraction. This sp^3 content is essential for ensuring the chemical inertness and hardness of the coating [14].

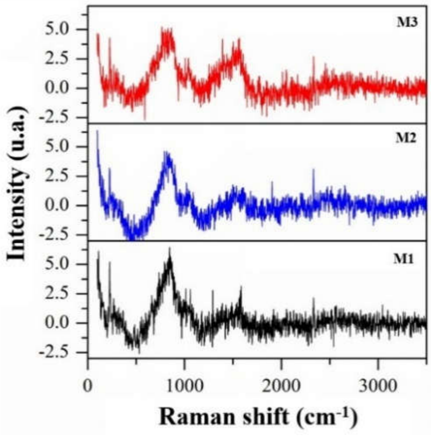

Figure 1. Raman spectra of samples M1 (incoming material), M2 (heat-treated sample) and M3 (DLC coating).

Figure 2 illustrates the cross-sectional view of the DLC coating, revealing a homogeneous and compact thickness deposited uniformly across the substrate. These characteristics align with previous studies reporting an absence of porosity, cracks, or defects factors that are instrumental in ensuring an effective chemical barrier. Furthermore, the substrate–coating interface exhibits optimal interfacial adhesion, a critical condition for mitigating delamination under dynamic loading and rolling contact fatigue [15].

doi:10.20944/preprints202604.2121.v1

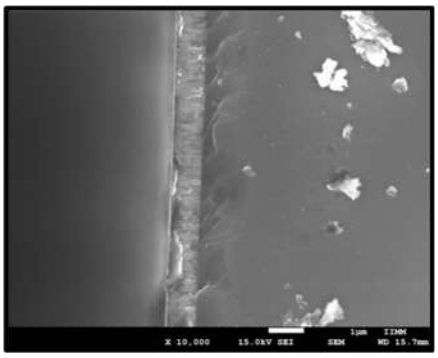

Figure 2. Cross-section micrograph of the DLC coating deposited on a silicon substrate.

3.2. Potentiodynamic Polarization Test

Potentiodynamic polarization tests were performed after the initial corrosion potential reached a stable value, with a stabilization period of approximately 20 min Figure 3 illustrates the potentiodynamic polarization curves for the studied alloys. Table 3 summarizes the corrosion potential (E_{corr}) and corrosion current density (i_{corr}) values obtained via the Tafel extrapolation method. The Tafel slopes were determined by linear fitting of the potentiodynamic polarization data within a range of ±150 mV relative to the E_{corr}.

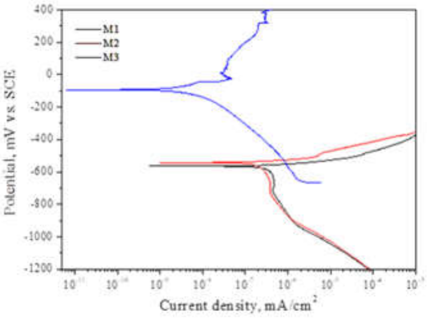

Figure 3. Potentiodynamic polarization curves.

Table 3. Electrochemical parameters obtained from potentiodynamic polarization tests.

Sample	E_{corr} (mV)	I_{corr} (mA/cm²)	βa (mV/decade)	βc (mV/decade)
M1	-564.43	$1.807\text{x}10^{-7}$	67	270
M2	-543.02	$1.000\text{x}10^{-7}$	80	240
M3	-91.5	$1.031\text{x}10^{-9}$	142	116

The analysis of the potentiodynamic polarization curves reveals a significant transition in the anodic dissolution mechanisms and corrosion kinetics following the deposition of the diamond-like carbon (DLC) coating onto the 52100-steel substrate. In this regard, the curves for M1 and M2 exhibit active dissolution behavior with no evidence of secondary passivation. These samples are characterized by high corrosion current densities (i_{corr}) and corrosion potentials (E_{corr}) that shift toward more active values after heat treatment, suggesting an alteration in the reactivity of the metallic surface [10,16,17]. Nevertheless, the intrinsic vulnerability of 52100 steel in aggressive media is evidenced by the anodic slope, which indicates a facilitated charge transfer toward the electrolyte [16]. In contrast, M3 exhibits a drastic reduction in current density by several orders of magnitude, thereby confirming its efficiency as a high-impedance barrier [18]. The shift of the corrosion potential toward more noble values demonstrates that the DLC coating effectively limits the diffusion of oxidizing species toward the substrate–coating interface [17]. The absence of reactivation peaks in the anodic branch for M3 indicates a compact, defect-free coating that prevents the formation of galvanic micro-cells or pitting, thereby optimizing the electrochemical durability of the system in saline environments [10,17].

3.3. Long-Term Tests

The evaluation results in synthetic seawater for the 52100 steel, the heat-treated 52100 steel, and the DLC coating obtained by LPR are presented through the corrosion rate kinetics and corrosion potential. Figure 4 illustrates that the variation of the corrosion potential (E_{corr}) is a function of time. The E_{corr} behavior for M1 exhibits an electrochemical response characteristic of an active dissolution system in an aggressive electrolytic medium. Initially, a rapid decrease toward highly active values is observed, indicating the inherent low chemical inertness of the AISI 52100 steel in its untreated microstructural state [19]. This condition stems from microstructural heterogeneity and the absence of a stable passivation layer, thereby facilitating the anodic dissolution of the surface. Throughout the 24 h exposure period, the E_{corr} values for M1 exhibit a generalized trend toward even more active potentials, which is indicative of a uniform corrosion process [19,20]. The observed fluctuations for M1 reflect a dynamic competition at the electrode–electrolyte interface, where the attempts to form transient corrosion products are outweighed by the dissolution rate and the breakdown of incipient passive layers induced by the presence of Cl^- ions [20].

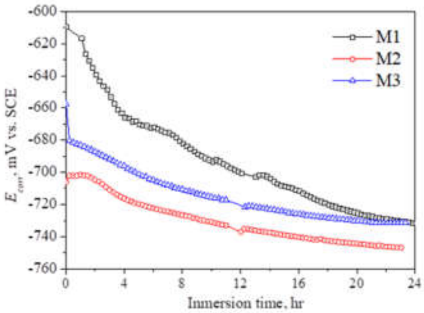

Figure 4. E_{corr} diagram of samples M1, M2 and M3.

The behavior of the E_{corr} values for M1 aligns with the morphology observed in the photomicrograph (Figure 5), where the M1 surface exhibits severe degradation characteristic of uniform corrosion, manifesting as excessive surface roughness and the formation of corrosion products. In the as-received condition of M1, the absence of surface treatment results in a microstructure rich in pre-existing local anodic sites, which promotes a high and homogeneous chemical attack rate across the entire surface [19]. The visible corrosion products act as partial and unstable diffusion barriers; far from passivating the surface, they exacerbate local degradation through differential aeration mechanisms and electrolyte entrapment, thus perpetuating the decline in corrosion potential observed in Figure 4 [20].

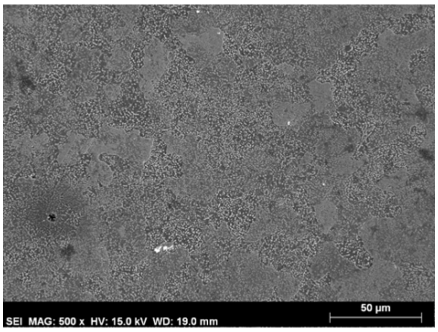

doi:10.20944/preprints202604.2121.v1

Figure 5. Photomicrographs of the surface of sample M1 with uniform corrosion.

For M2, the E_{corr} values (Figure 4) reveal a complex dynamic response compared to the steel in its as-received state (M1), which is attributable to the microstructural modifications induced by the heat treatment. During the initial hours of immersion, M2 exhibits a more stable E_{corr} than M1, suggesting enhanced chemical inertness or the formation of stable temporary passive layers, likely due to phase homogenization and the reduction of crystalline defects resulting from the treatment [21]. However, after 5 h of exposure, the E_{corr} of M2 undergoes a downward trend toward more active values, indicative of surface activation and accelerated anodic dissolution of the steel [22]. The fluctuations observed for M2 reflect an unstable electrochemical competition at the electrode–electrolyte interface, where local dissolution competes with the transient formation of corrosion products that fail to effectively passivate the surface [21,22].

The surface of sample M2 (Figure 6) exhibits severe degradation, characterized by a heavy presence of generalized corrosion products accumulated at specific sites. The morphology of these products suggests that the heat treatment, while improving the initial microstructure, was insufficient to prevent the penetration of aggressive agents—such as Cl^- ions into the substrate [21]. These corrosion products act as partial and unstable diffusion barriers; far from providing protection, they exacerbate local degradation through differential aeration mechanisms and electrolyte entrapment, thereby perpetuating the downward E_{corr} trend observed in Figure 4 [22].

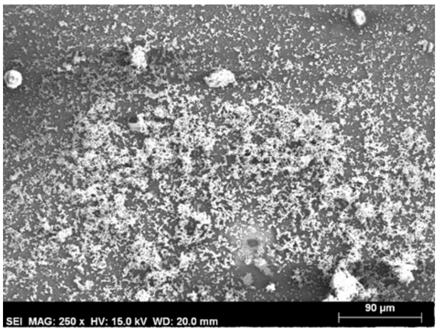

Figure 6. Photomicrographs of the surface of sample M2 showing the presence of corrosion products.

Sample M3 (Figure 4) evidences superior thermodynamic stability and significantly mitigated corrosion kinetics (Figure 8) compared to samples M1 and M2. The E_{corr} for M3 is positioned at notably more noble values from the onset of immersion, which is indicative of the diamond-like carbon (DLC) film characteristics; specifically, it acts as a quasi-insulating physical barrier against the aggressive electrolyte [10,23,24]. The absence of a downward trend during the immersion period confirms that the coating effectively prevents Cl^- penetration toward the steel interface, thereby maintaining the electrochemical integrity of the system [2]. Nevertheless, the minor fluctuations observed in the M3 curve, in conjunction with the morphology presented in Figure 7, suggest the onset of a localized degradation process. The flaking of corrosion products observed in the micrograph of Figure 7 is attributable to a subsurface corrosion mechanism at sites where intrinsic micro-defects exist within the DLC film [23]. At these locations, the formation of corrosion products at the substrate–coating interface generates internal stresses that exceed the interfacial adhesion strength, leading to the lifting and subsequent detachment of the protective layer [24]. This flaking phenomenon is critical, as the loss of coating continuity exposes local anodic areas; however, the potentials exhibit a more noble behavior compared to the bare substrate due to the vast remaining area that still retains its passive and protective character [10,24].

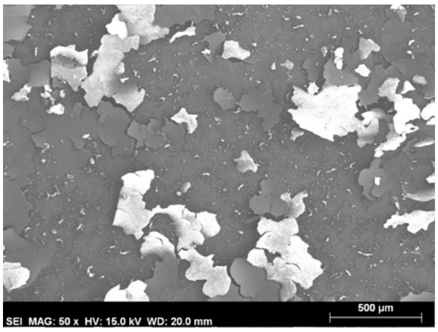

Figure 7. Photomicrographs of the surface of sample M3 show flaking of corrosion products.

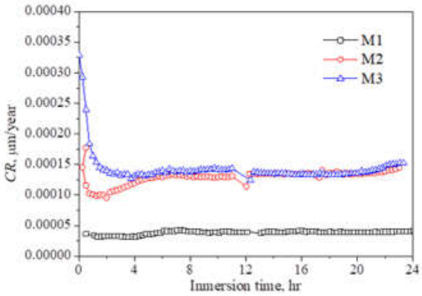

Figure 8. Corrosion rates of samples M1, M2 and M3 after 24 hours of immersion in a synthetic seawater solution.

The electrochemical behavior analysis of the DLC coating system deposited via HiPIMS on AISI 52100 steel in synthetic seawater reveals a temporal evolution of the total porosity P, highlighting the complexity of the protection mechanisms at the inert–active interface. The total porosity was determined using the equation proposed by Creus et al. [25]:

$$P = (R_{ps}/R_p)\text{x}10^{-(\Delta E_{corr}/\beta a)}, \quad (6)$$

Where R_{ps} represents the polarization resistance of the bare substrate, R_p denotes the polarization resistance of the DLC coating, ΔE_{corr} is the corrosion potential shift, and βa is the anodic Tafel slope of the DLC coating.

Table 4. Electrochemical characteristics of coated steel after 12 and 24 hours of immersion in a synthetic seawater solution and determination of porosity P by the polarization resistance method.

Sample	Rp_s (Ω·cm²)	Rp (Ω·cm²)	E^{steel}_{corr} (mV)	E_{corr} (mV)	βa (mV/decade)	P (%)
DLC_{12}	6359.7	2389.4	-700.62	-721.57	142	3.73
DLC_{24}	6045.3	1953.1	-731.88	-731.33	142	3.06

The obtained values show a transition from P = 3.73% at 12 h of immersion to P = 3.06% at 24 h. This decrease in porosity values corresponds to the kinetics of formation and accumulation of corrosion products within the micro-channels and intrinsic defects of the DLC coating. Despite the high chemical inertness and hardness of the coating, seawater penetration through open pores is not prevented, thereby activating local galvanic cells at the base of the defects [26]. The volumetric expansion of these subproducts (oxides/hydroxides) creates a physical obstruction that increases the charge transfer resistance of the system, thus reducing the apparent porosity. This phenomenon is particularly relevant for AISI 52100 steel, where the martensitic microstructure and phase distribution influence the stability of the corrosion-induced passivation layer at the pore bottom [27]. Consequently, the system exhibits a transient self-limiting corrosion mechanism mediated by the blockage of ionic diffusion paths; however, the persistence of porosity levels above 3% serves as a warning regarding the risk of localized delamination due to interfacial stresses during prolonged exposure.

The surface of sample M3 after exposure (Figure 9) reveals zones with discrete porosities and corrosion craters following 24 h of immersion, thereby validating the total porosity calculations. The presence of these defects after the HiPIMS deposition process provides preferential diffusion channels for Cl^- ions, triggering localized corrosion processes at the substrate–coating interface. According to Creus et al. [25], the P = 3.06% value at 24 h is physically manifested in these discontinuities, where the formation of corrosion products within the pores can induce tensile stress that compromises the coating cohesion. This intrinsic vulnerability of AISI 52100 steel whose martensitic microstructure and carbide distribution may generate heterogeneities during coating nucleation, facilitates the appearance of "pinholes" as previously described by Jovičević-Klug et al. [27]. In this regard, the observed morphology aligns with current challenges in surface engineering for tribocorrosion applications discussed by Wang et al. [26], where coating density is the determining factor in mitigating the formation of local galvanic cells which, as seen in Figure 9, initiate the structural degradation process of the system.

Figure 9. Photomicrographs of the surface of M3, after 24 hours of immersion.

3.4. EIS Test

The electrochemical behavior of M1 (52100 steel) after 24 h of immersion exhibits a charge transfer resistance (R_{ct}) significantly higher than those of M2 and M3, evidenced by a capacitive loop in the Nyquist plot extending up to 3500 $\Omega \cdot cm^2$. This response suggests a mixed control regime, initially dominated by species diffusion across the metal/electrolyte interface and evolving toward a pseudocapacitive state as the corrosion product layer stabilizes. This phenomenon is further confirmed by the Bode plot (Figure 11), where the maximum phase angle reaches approximately -70°, indicating that the formed film does not act as a purely capacitive insulator but rather as an electrochemically active interface. According to the photomicrograph and elemental mapping (Figure 12), the surface morphology reveals clusters of products enriched in Fe, O, and Cl, validating the formation of complex oxyhydroxides. The presence of Cl is indicative of akaganeite (β-FeOOH) nucleation, a characteristic product in marine environments whose formation follows the pathway described in Equation 7. Simultaneously, the Cr content (approx. 1.5%) in the 52100 steel promotes an interfacial enrichment that favors the formation of adsorbed chromium hydroxides (Equation 8), which are responsible for the pseudocapacitive behavior and the enhanced stability of the impedance arc [28,29].

$$8Fe^{+2}+Cl^{-}+12H_2O\rightarrow \beta\text{-}Fe_8O_8(OH)_{15}Cl+25H^{+}+16e^{-}, \tag{7}$$

$$Cr+3H_2O\rightarrow Cr(OH)_{3,ads}+3H^{+}+3e^{-}, \tag{8}$$

In this regard, the detection of Ca may be indicative of calcareous deposit ($CaCO_3$) precipitation resulting from the local pH increase generated by the cathodic oxygen reduction (Equation 9). These deposits act as sealants within pits or pores, restricting the diffusive flux of aggressive species toward the metallic substrate [30,31]. The synergy between the Cr-doped corrosion products and the calcareous scale (Equation 10) explains the magnitude of the total impedance and the pseudo-protection exhibited by M1 within the synthetic seawater environment.

$$O_2+2H_2O+4e^-, \tag{9}$$

$$Ca^{2+}HCO^{-}_{3}+OH^{-}\rightarrow CaCO_3+H_2O, \tag{10}$$

After 24 h of immersion in synthetic seawater, M2 exhibits a more active electrochemical performance. The Nyquist plot (Figure 10) displays a capacitive loop with a significantly reduced diameter, indicating a notably low charge transfer resistance (R_{ct}). This behavior points to a high rate of anodic dissolution at the interface, where the corrosion product layer fails to establish an effective protective barrier against the diffusion of aggressive ions [32,33]. Correspondingly, the Bode plot (Figure 11) shows that the phase angle shifts toward values below -60°, deviating from ideal capacitive behavior. Such a response is characteristic of surfaces with porous oxide films that facilitate the penetration of the medium toward the metallic substrate. Consequently, M2 fails to establish a defined time constant indicative of effective long-term protection, which is typical for steels with low corrosion resistance in Cl^--rich environments [10,34]. The photomicrograph (Figure 13) confirms the presence of chlorine and oxygen concentrations within the obtained corrosion products. The observed morphology suggests the predominant formation of akaganeite (β-FeOOH), whose lattice structure accommodates Cl^- ions, thereby promoting local acidification and the propagation of the attack as previously described (Equation 7) [35,36].

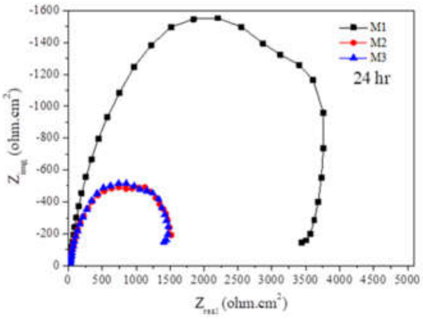

Figure 10. Electrochemical Impedance Spectroscopy Response of Samples After 24 hr Immersion in Synthetic Seawater.

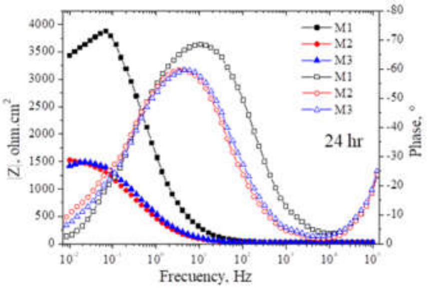

Figure 11. Bode plot of the samples after 24 hr immersion in synthetic seawater.

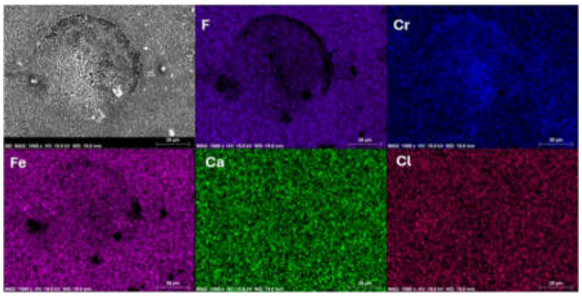

Figure 12. This is a figure. Schemes follow the same formatting.

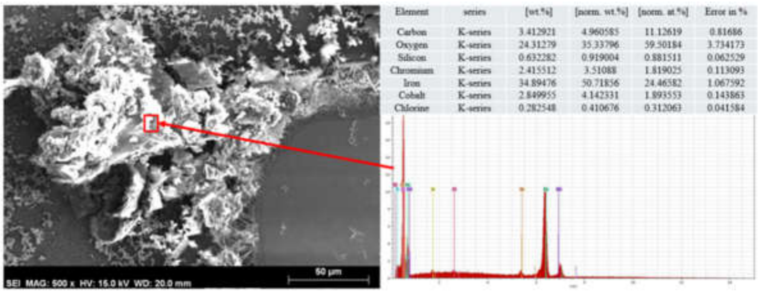

Element	series	[wt.%]	[norm. wt.%]	[norm. at.%]	Error in %
Carbon	K-series	3.412921	4.960585	11.12619	0.81686
Oxygen	K-series	24.31279	35.33796	59.50184	3.734173
Silicon	K-series	0.632282	0.919004	0.881511	0.062529
Chromium	K-series	2.415512	3.51088	1.819025	0.113093
Iron	K-series	34.89476	50.71856	24.46582	1.067592
Cobalt	K-series	2.849955	4.142331	1.893553	0.143863
Chlorine	K-series	0.282548	0.410676	0.312063	0.041584

Figure 13. Photomicrographs of M2 after 24 hours of immersion in a synthetic seawater solution, with analysis by energy dispersive X-ray spectroscopy (EDS).

In contrast to M1, where the precipitation of calcareous deposits ($CaCO_3$) acts as a pore sealant, the Ca distribution detected by EDS in M2 is insufficient to mitigate the diffusive flux [37]. In other words, the corrosion process in M2 is governed by low interfacial resistance and the presence of a chemically active oxide that fails to provide secondary passivity against the marine environment.

Figures 10 and 11 illustrate the capacitive behavior of M3 after 24 h of immersion in synthetic seawater. The Nyquist plot (Figure 10) for M3 shows a well-defined semicircular arc, which is characteristic of charge transfer resistance (R_{ct}) behavior. This response indicates that the DLC coating acts as an effective physical barrier against the infiltration of corrosive species (Cl^- and OH^-) present in the marine environment [38]. Correspondingly, the impedance values observed in the low-frequency region of the Bode plot (Figure 11) support the protective nature of the DLC. The chemical inertness of the sp^3-hybridized carbon matrix in these DLC films provides a high degree of electrochemical resistance, effectively decoupling the metallic substrate from the electrolyte [38]. Furthermore, the phase angle for M3 in the Bode plot (Figure 11) exhibits an amplitude approaching -60° over a wide frequency range. This response suggests the presence of at least two overlapping time constants: one associated with the DLC coating properties (CPE_{coat}) and another related to the electrochemical double layer at the coating/substrate interface (CPE_{dl}) [39]. The stability of this phase angle after 24 h suggests that the coating maintains its structural integrity without significant electrolyte seepage through macropores or defects.

Figure 14 presents the surface morphology and X-ray mapping of sample M3 following the corrosion test. The micrograph reveals a predominantly smooth and dense surface, characteristic of coatings deposited via High-Power Impulse Magnetron Sputtering (HiPIMS). The application of this technique promotes high ionization of the sputtered species, leading to denser amorphous carbon structures with fewer defects compared to alternative methods; the homogeneous and dense carbon distribution in the mapping confirms the formation of a continuous DLC matrix, in agreement with previous studies [40]. The presence of Fe and Cr originates from the substrate and the chromium interlayer employed for the mechanical adhesion of the coating to the AISI 52100 steel, indicating that the coating thickness and density are sufficient to mitigate diffusion and subsequent corrosion product formation. As noted in prior research, enhanced adhesion and density achieved through pre-treatments drastically reduce diffusion pathways [41]. In this regard, the uniformly distributed

Preprints.org (www.preprints.org) | NOT PEER-REVIEWED | Posted: 30 April 2026 doi:10.20944/preprints202604.2121.v1

oxygen observed within the context of synthetic seawater immersion does not necessarily indicate coating failure; instead, it may point to the adsorption of species from the medium or the formation of an extremely thin passive layer at sites where the electrolyte reaches the interface. Nevertheless, the presence of specific zones with higher Fe and O concentrations suggests the initiation of localized corrosion processes, while maintaining the chemical integrity previously discussed [39].

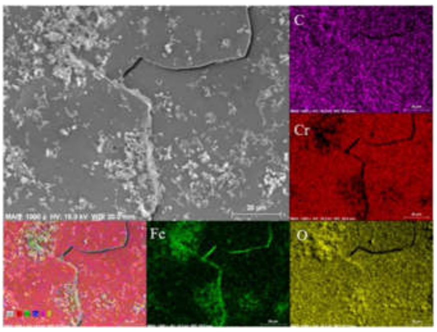

Figure 14. Photomicrographs of M3 after 24 hours of immersion in a synthetic seawater solution, with X-ray mapping.

The chemical stability observed in Figure 14 agrees with the obtained EIS results (Figures 10 and 11), where the ability of M3 to exhibit an EDS spectrum with negligible accumulation of corrosion products (iron oxides) confirms the high impermeability of the DLC physical barrier. This behavior is consistent with previous studies, which demonstrated that high-density amorphous carbon coatings provide long-term protection by effectively blocking active sites against Cl^- attack [42].

4. Discussion

A critical aspect for a comprehensive understanding of the electrochemical behavior of the HiPIMS-deposited DLC coating is the interaction between intrinsic residual stresses and the electrochemical response determined via EIS. In this regard, Raman analysis suggests the presence of high compressive stresses within the film, derived from the G-band shift toward higher wavenumbers—a characteristic feature of these coatings densified by ion bombardment [43–45]. The estimation of residual stress can be expressed as:

$$\sigma = k(\omega_G - \omega_0), \qquad (11)$$

Where K represents the Raman sensitivity constant and $(\omega_G - \omega_0)$ denotes the G-band shift relative to unstressed carbon. This approach allows for the inference of compressive stresses in the range of -3 to -4 GPa, which are consistent with DLC coatings obtained via HiPIMS [45–47]. For the present study, the unstressed peak position is taken as ω_0 = 1580 cm^{-1}, with an observed value of ω_G = 1592 cm^{-1} and a Raman sensitivity constant ranging from -0.25 to -0.35 GPa/cm^{-1}.

$$\sigma = -0.3(1592 - 1580) = -3.6 \text{ GPa}, \qquad (12)$$

From an electrochemical standpoint, these compressive stresses exert a direct influence on the coating microstructure, promoting enhanced densification and reducing defect connectivity. This results in a significant increase in polarization resistance, which is related to i_{corr} through the Stern–Geary equation. In this context, the increase in polarization resistance (Rp) observed for M3 is directly associated with reduced coating permeability, thereby limiting the transport of aggressive species, such as Cl^-, toward the substrate-coating interface [23,42]. Additionally, the EIS response can be modeled using an equivalent electrical circuit (Figure 15) that accounts for the contributions of both the coating and the electrochemical double layer.

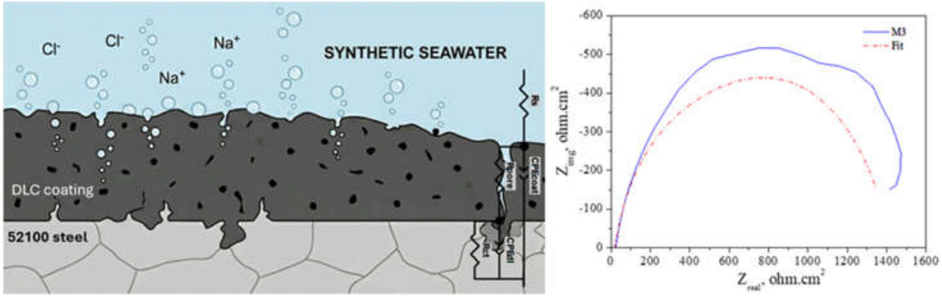

Figure 15. Equivalent electrical circuit used to simulate the EIS data of the DLC coating and Nyquist diagram with the fitted curve.

Table 5. Adjustment parameters used to simulate the EIS data of the DLC coating in synthetic seawater.

Sample	*Rs* (*Ω·cm²*)	*R_{pore}* (*Ω·cm²*)	*CPE_{coat}* (*F/cm²*)	*R_{ct}* (*Ω·cm²*)	*CPEdl* (*F/cm²*)
M3	20.7	635	3 x 10^{-5}	1450	7 x 10^{-5}

Where Rs is the electrolyte resistance, Rpore represents the resistance of the coating pores or defects, CPEcoat is the constant phase element of the coating, Rct denotes the charge transfer resistance, and CPEdl is the constant phase element of the substrate-coating double layer (Figure 15). The presence of two time constants observed in the Bode plot confirms the existence of these two coupled processes, which is characteristic of dense DLC coatings [39]. However, the EIS behavior and porosity values reveal that the coating protection is not absolute. The obtained values of P = 3.73% after 12 h of immersion and P = 3.06% after 24 h indicate that, despite the high densification induced by compressive stresses, defects persist and act as preferential pathways for electrolyte penetration.

In this context, residual stresses play a dual role. On the one hand, they contribute to the enhancement of the coating's barrier performance by increasing Rpore and Rct values, as evidenced by the impedance modules in the low-frequency region. On the other hand, the accumulation of elastic energy within the film promotes stress concentration at local defects, which may induce delamination processes when coupled with the formation of corrosion products at the interface [24,44].

This phenomenon can be explained by considering that the penetration of aggressive species through pores, triggers electrochemical reactions at the interface yielding iron oxides and hydroxides with a higher molar volume than the substrate. The associated volumetric expansion increases local stresses, exceeding the coating's adhesive strength and promoting its detachment. This mechanism is consistent with the observed morphology and the evolution of porosity, which provide evidence of a partial sealing effect of defects due to the accumulation of corrosion products, albeit without completely eliminating localized degradation [26,45].

5. Conclusions

The present study comprehensively demonstrates that the deposition of diamond-like carbon (DLC) coatings via High-Power Impulse Magnetron Sputtering (HiPIMS) is highly effective in enhancing the electrochemical corrosion resistance of AISI 52100 steel in simulated marine environments. A homogeneous and dense coating with adequate interfacial adhesion was achieved, characterized by a microstructure composed of sp^2/sp^3 bonding. Raman spectroscopy allowed for the quantification of high compressive residual stresses, which directly correlate with coating densification, a key factor in improving its barrier properties. From an electrochemical perspective, the DLC coating induced a significant reduction in i_{corr} and a shift of E_{corr} towards more noble values, evidencing a clear mitigation of anodic dissolution processes. This behavior confirms that the DLC acts as an effective physical barrier, limiting the diffusion of aggressive species such as Cl^-.

EIS results revealed a substantial increase in Rct and low-frequency impedance modulus values, accompanied by the emergence of two time constants associated with the coating and the electrochemical double layer, respectively. This response confirms a coupled protection mechanism, where coating integrity and interfacial stability act synergistically. A significant finding is the dynamic evolution of the coating porosity, which decreased from 3.73% to 3.06% over immersion time. This phenomenon is attributed to a self-sealing mechanism induced by the accumulation of corrosion products within defects and microchannels, further increasing Rct. However, the protection was found to be non-absolute; intrinsic defects (pinholes) serve as preferential sites for the initiation of localized corrosion at the substrate-coating interface. The formation of corrosion products at these sites generates internal stresses that can induce delamination, highlighting the dual role of residual stresses: beneficial for densification but potentially critical for long-term stability. Finally, the thermal treatment of M2 showed limited improvement compared to the base material, failing to establish effective protection against the aggressive medium, which underscores the coating as the primary protective mechanism.

The correlation between residual stresses (Raman), electrochemical response (EIS), and porosity establishes that DLC coating performance is governed by a balance between structural densification and mechanical stability. Consequently, optimizing HiPIMS deposition parameters is fundamental to controlling residual stress levels, minimizing defect formation, and maximizing system durability in aggressive environments.

Author Contributions: Conceptualization, I.A., E.H. and A.M.; writing—original draft preparation I.A., E.H. and A.M.; formal analysis, I.A., E.H., M.F. and A.M; writing—review and editing, A.M. and H.C.; methodology E.H. and J.B.; validation, M.F. and A.M.; resources, E.H., M.F., J.B., H.C. and A.M. All authors have read and agreed to the published version of the manuscript.

Funding: This research received no external funding.

Data Availability Statement: The data presented in this study are available on request from the corresponding author due to privacy.

Acknowledgments: I.A. wish to express her gratitude to the Secretariat of Science, Humanities, Technology and Innovation (Secihti) for the scholarship received during her postgraduate studies. The authors of this article wish to express their gratitude to the Materials Degradation Laboratory of the FIM-UMSNH for the support provided. During the preparation of this manuscript, the authors used Gemini AI as a translation tool from Spanish to English.

Conflicts of Interest: The authors declare no conflicts of interest.

Abbreviations

The following abbreviations are used in this manuscript:

HiPIMS	High-Power Impulse Magnetron Sputtering
DLC	Diamond-like carbon
LPR	Linear polarization resistance
EIS	Electrochemical impedance spectroscopy
PVD	Physical Vapor Deposition
W-DLC	Tungsten-doped diamond-like carbon
PIII	Plasma Immersion Ion Implantation
M1	Sample As-received condition 52100 steel
M2	Samples underwent a hardening heat treatment
M3	Sample covered diamond-like carbon (DLC) coating
SEM	Scanning Electron Microscope
EDS	Energy Dispersive X-ray Spectroscopy
SCE	Saturated calomel electrode
OCP	Open circuit potential

ASTM	American Society for Testing and Materials
FWHM	Full width at half maximum

References

1. Mannens, R.; Uhlmann, L.; Lambers, F.; Feuerhack, A.; Bergs, T. Surface Integrity of AISI 52100 Bearing Steel after Robot-Based Machine Hammer Peening. J. Manuf. Mater. Process. 2020, 4, 61. https://doi.org/10.3390/jmmp4020061
2. Zmarzły, P. Analysis of Technological Heredity in the Production of Rolling Bearing Rings Made of AISI 52100 Steel Based on Waviness Measurements. Materials 2022, 15, 3959. https://doi.org/10.3390/ma15113959
3. Kao, W.H.; Su, Y.L.; Shih, M.Y. Effects of Varying Power and Argon Gas Flux on Tribological Properties and High-Speed Drilling Performance of Diamond-Like Carbon Coatings Deposited using High-Power Impulse Magnetron Sputtering System. J. Mater. Eng. Perform. 2021, 30, 6485–6499. https://doi.org/10.1007/s11665-020-05242-6
4. Li, Y.; Jiang, Z.; Li, L.; Wang, P.; Li, D.; Xue, W.; Duan, D. Wear behavior and damage characterization for AISI 52100 bearing steels: Effect of hardness and spherical carbides. J. Mater. Res. Technol. 2024, 30, 8359–8370. https://doi.org/10.1016/j.jmrt.2024.05.220
5. García, J.A.; Rivero, P.J.; Barba, E.; Fernández, I.; Santiago, J.A.; Palacio, J.F.; Fuente, G.G.; Rodríguez, R.J. A Comparative Study in the Tribological Behavior of DLC Coatings Deposited by HiPIMS Technology with Positive Pulses. Metals 2020, 10, 174. https://doi.org/10.3390/met10020174
6. Rashid, M.M.-U.; Tomkowski, R.; Archenti, A. Effect of Surface Pre-Treatment on the Adhesion between HiPIMS Thick Cu:CuCNx Coating and WC-Co Shim. Coatings 2022, 12, 1484. https://doi.org/10.3390/coatings12101484
7. Wu, L.; Bai, Z.; Hao, Q.; Qin, J. Improving Wear Resistance of DLC-Coated Metal Components During Service: A Review. Lubricants 2025, 13, 257. https://doi.org/10.3390/lubricants13060257
8. Farooq, S.A.; Raina, A.; Mohan, S.; Arvind Singh, R.; Jayalakshmi, S.; Irfan Ul Haq, M. Nanostructured Coatings: Review on Processing Techniques, Corrosion Behaviour and Tribological Performance. Nanomaterials 2022, 12, 1323. https://doi.org/10.3390/nano12081323
9. Shaikh, S.; Sadeghi, M.; Cruz, S.; Ferreira, F. Recent Progress on the Tribology of Pure/Doped Diamond-like Carbon Coatings and Ionic Liquids. Coatings 2024, 14, 71. https://doi.org/10.3390/coatings14010071
10. Vicen, M.; Kajánek, D.; Trško, L.; Bokůvka, O.; Buchtík, M.; Florková, Z.; Frkáň, M. Improving of 100Cr6 Steel Corrosion and Wear Properties in Simulated Sea Water Environment by Tungsten-Doped DLC Coating. Materials 2023, 16, 4334. https://doi.org/10.3390/ma16124334
11. Gómez, I.; Claver, A.; Santiago, J.A.; Fernandez, I.; Palacio, J.F.; Diaz, C.; Mändl, S.; Garcia, J.A. Improved Adhesion of the DLC Coating Using HiPIMS with Positive Pulses and Plasma Immersion Pretreatment. Coatings 2021, 11, 1070. https://doi.org/10.3390/coatings11091070
12. Bhaumik, S.; Paleu, V. Wear and Rolling Contact Fatigue Analysis of AISI 52100 Bearing Steel in Presence of Additivated Lubricants. Metals 2021, 11, 907. https://doi.org/10.3390/met11060907
13. Hassan, M.; Qayyum, A.; Ahmad, S.; Mahmood, S.; Shafiq, M.; Zakaullah, M.; Lee, P.; Rawat, R.S. DLC coating on stainless steel by pulsed methane discharge in repetitive plasma focus. Appl. Surf. Sci. 2014, 303, 187–195. https://doi.org/10.1016/j.apsusc.2014.02.142
14. He, M.; Yeo, C. Evaluation of Thermal Degradation of DLC Film Using a Novel Raman Spectroscopy Technique. Coatings 2018, 8, 143. https://doi.org/10.3390/coatings8040143
15. Piotrowska, K.; Madej, M.; Milewski, K. Tribological Properties of DLC Coatings in Model-Based and Real-Life Tests. Materials 2025, 18, 4251. https://doi.org/10.3390/ma18184251
16. Yan, Y.; Zhu, Y.; Zhang, L.; Zou, C.; Hu, Z.; Zhou, H.; Cai, L. Study on the anodic behavior of AISI E52100 steel in two fluorine-containing ionic liquids. Res. Chem. Intermed. 2021, 47, 2107–2123. https://doi.org/10.1007/s11164-020-04386-3
17. Metel, A.; Sotova, C.; Fyodorov, S.; Zhylinski, V.; Chayeuski, V.; Milovich, F.; Seleznev, A.; Bublikov, Y.; Makarevich, K.; Vereschaka, A. Improving the Wear and Corrosion Resistance of Titanium Alloy Parts via the Deposition of DLC Coatings. C 2024, 10, 106. https://doi.org/10.3390/c10040106

18. Fenili, C.P.; de Souza, F.S.; Marin, G.; Probst, S.M.H.; Binder, C.; Klein, A.N. Corrosion resistance of low-carbon steel modified by plasma nitriding and diamond-like carbon. Diam. Relat. Mater. 2017, 80, 153–161. https://doi.org/10.1016/j.diamond.2017.11.001
19. Wang, W.; Srinivasan, V.; Siva, S.; Albert, B.; Lal, M.; Alfantazi, A. Corrosion Behavior of Deep Cryogenically Treated AISI 420 and AISI 52100 Steel. Corrosion 2014, 70, 708–720. https://doi.org/10.5006/1150
20. Jin, K.; Qiao, Z.; Wang, S.; Zhu, S.; Cheng, J.; Yang, J.; Liu, W. The effects of main components of seawater on the tribological properties of Cu-9Al-5Ni-4Fe-Mn alloy sliding against AISI 52100 steel. RSC Adv. 2016, 6, 25528–25542. https://doi.org/10.1039/C5RA19719H
21. Wang, D.; Zhao, Q.; Yang, T.; Chang, X.; Qu, S.; Sun, S.; Gao, S.; Zhang, C.; Lu, X.; Yin, Y. Influences of Thermomechanical Conditions on Corrosion Behavior of low-carbon steels in Artificial Seawater. Int. J. Electrochem. Sci. 2019, 14, 2509–2525. https://doi.org/10.20964/2019.03.65
22. Xie, J.; Alpas, A.T.; Northwood, D.O. The role of heat treatment on the erosion-corrosion behavior of AISI 52100 steel. Mater. Sci. Eng. A 2005, 393, 42–50. https://doi.org/10.1016/j.msea.2004.09.045
23. Lupu, F.C.; Munteanu, C.; Müftü, S.; Benchea, M.; Cimpoesu, R.; Ferguson, G.; Boese, S.; Schwartz, P.; Istrate, B.; Arsenoaia, V.N. Evaluation of the Wear Properties and Corrosion Resistance of 52100 Steel Coated with Ni/CrC by Cold Spraying. Coatings 2024, 14, 145. https://doi.org/10.3390/coatings14010145
24. Cao, L.; Liu, J.; Wan, Y.; Pu, J. Corrosion and tribocorrosion behavior of W doped DLC coating in artificial seawater. Diam. Relat. Mater. 2020, 109, 108019. https://doi.org/10.1016/j.diamond.2020.108019
25. Creus, J.; Mazille, H.; Idrissi, H. Porosity evaluation of protective coatings onto steel, through electrochemical techniques. Surf. Coat. Technol. 2000, 130, 224–232. https://doi.org/10.1016/S0257-8972(99)00659-3
26. Wang, Y.; Feng, C.; Lin, T.; Zhu, R.; Zhang, J.; Yang, H.; Yi, S.; He, J.; Tu, M.; Wei, G. A Review of Wear-Resistant Coatings for Steel Substrates: Applications and Challenges. Metals 2025, 15, 1231. https://doi.org/10.3390/met15111231
27. Jovičević-Klug, P.; Kranjec, T.; Jovičević-Klug, M.; Kosec, T.; Podgornik, B. Influence of the Deep Cryogenic Treatment on AISI 52100 and AISI D3 Steel's Corrosion Resistance. Materials 2021, 14, 6357. https://doi.org/10.3390/ma14216357
28. Yuan, J.; Li, P.; Zhang, H.; Yin, S.; Xu, M. Electrochemical Characteristics and Corrosion Mechanisms of High-Strength Corrosion-Resistant Steel Reinforcement under Simulated Service Conditions. Metals 2024, 14, 876. https://doi.org/10.3390/met14080876
29. Zhang, G.; Zhang, H.; Liu, X.; Xin, Y.; Yin, S.; Gao, L.; Shi, Z. Effect of Mn on Corrosion Resistance of Low-Cr Weathering Steel. Metals 2024, 14, 1433. https://doi.org/10.3390/met14121433
30. Sun, T.; Huang, G.; Lv, P.; Xu, L.; Ma, L. Evolution of Calcareous Deposits and Passive Film on 304 Stainless Steel with Cathodic Polarization in Sea Water. Coatings 2018, 8, 194. https://doi.org/10.3390/coatings8050194
31. Yang, Y.; Scantlebury, J.D.; Koroleva, E.V. A Study of Calcareous Deposits on Cathodically Protected Mild Steel in Artificial Seawater. Metals 2015, 5, 439–456. https://doi.org/10.3390/met5010439
32. Zhang, H.; Yan, L.; Zhu, Y.; Ai, F.; Li, H.; Li, Y.; Jiang, Z. The Effect of Immersion Corrosion Time on Electrochemical Corrosion Behavior and the Corrosion Mechanism of EH47 Ship Steel in Seawater. Metals 2021, 11, 1317. https://doi.org/10.3390/met11081317
33. Jiang, X.; Zhou, Y.; Shi, C.; Mao, D. Effects of Ultrasonic-Aided Quenching on the Corrosion Resistance of GB 35CrMoV Steel in Seawater Environment. Metals 2018, 8, 104. https://doi.org/10.3390/met8020104
34. Zhao, L.; He, W.; Wang, Y.; Li, H.; Cui, Z. A Comparative Study of the Corrosion Behavior of 30CrMnSiNi2A in Artificial Seawater and Salt Spray Environments. Metals 2022, 12, 1443. https://doi.org/10.3390/met12091443
35. Yang, Y.; Lin, T.; Wang, G.; Wang, Y.; Shao, M.; Meng, F.; Wang, F. Corrosion Behaviors of Weathering Steels in the Actual Marine Atmospheric Zone and Immersion Zone. Metals 2024, 14, 903. https://doi.org/10.3390/met14080903
36. Khazaal, S.H.; Makki, H.F. Comprehensive Review on Carbon Steels Corrosion in Chloride-Rich Media. J. Chem. Pet. Eng. 2025, 59, 357–385. 10.22059/jchpe.2025.393259.1613

doi:10.20944/preprints202604.2121.v1

37. Li, Z.L.; Xiao, K.; Dong, C.F.; Cheng, X.Q.; Xue, W.; Yu, W. Atmospheric corrosion behavior of low-alloy steels in a tropical marine environment. J. Iron Steel Res. Int. 2019, 26, 1184–1195. https://doi.org/10.1007/s42243-019-00316-9
38. Sharma, R.; Barhai, P.K.; Kumari, N. Corrosion resistant behaviour of DLC films. Thin Solid Films 2008, 516, 5397–5403. https://doi.org/10.1016/j.tsf.2007.07.099
39. Kolanji, S.; Sivakatatcham, M.; Palani, S. Studies on Nano-Indentation and Corrosion Behavior of Diamond-Like Carbon Coated Stainless Steel (316L). Trends Sci. 2024, 21, 7677. https://doi.org/10.48048/tis.2024.7677
40. Ganesan, R.; Fernandez-Martinez, I.; Akhavan, B.; Matthews, D.T.A.; Sergachev, D.; Stueber, M.; McKenzie, D.R.; Bilek, M.M.M. Pulse length selection in bipolar HiPIMS for high deposition rate of smooth, hard amorphous carbon films. Surf. Coat. Technol. 2023, 454, 129199. https://doi.org/10.1016/j.surfcoat.2022.129199
41. Gómez, I.; Claver, A.; Santiago, J.A.; Fernandez, I.; Palacio, J.F.; Diaz, C.; Mändl, S.; Garcia, J.A. Improved Adhesion of the DLC Coating Using HiPIMS with Positive Pulses and Plasma Immersion Pretreatment. Coatings 2021, 11, 1070. https://doi.org/10.3390/coatings11091070
42. Li, S.; Li, H.; Guo, P.; Li, X.; Yang, W.; Ma, G.; Nishimura, K.; Ke, P.; Wang, A. Enhanced Long-Term Corrosion Resistance of 316L Stainless Steel by Multilayer Amorphous Carbon Coatings. Materials 2024, 17, 2129. https://doi.org/10.3390/ma17092129
43. Ferrari, A.C.; Robertson, J. Interpretation of Raman spectra of disordered and amorphous carbon. Phys. Rev. B 2000, 61, 14095–14107. https://doi.org/10.1103/PhysRevB.61.14095
44. Robertson, J. Diamond-like amorphous carbon. Mater. Sci. Eng. R Rep. 2002, 37, 129–281. https://doi.org/10.1016/S0927-796X(02)00005-0
45. Grill, A. Diamond-like carbon: state of the art. Diamond Relat. Mater. 1999, 8, 428–434. https://doi.org/10.1016/S0925-9635(98)00262-3
46. Lifshitz, Y. Diamond-like carbon: present status. Diamond Relat. Mater. 1999, 8, 1659–1676. https://doi.org/10.1016/S0925-9635(99)00087-4
47. Casiraghi, C.; Ferrari, A.C.; Robertson, J. Raman spectroscopy of hydrogenated amorphous carbons. Phys. Rev. B 2005, 72, 085401. https://doi.org/10.1103/PhysRevB.72.085401